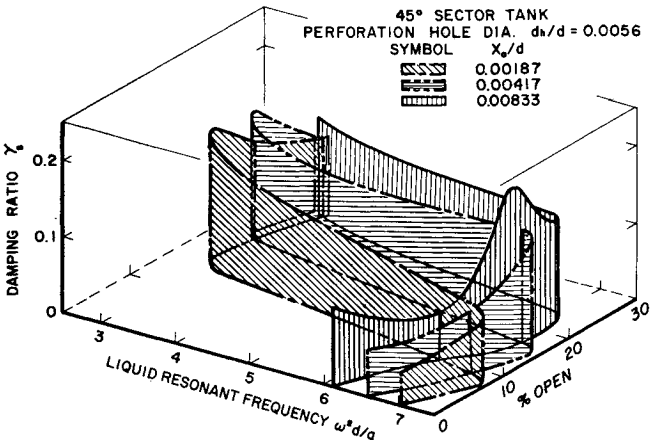

Fig. 4 Variation in damping ratio for 45° sector tank.

affecting the damping, failed to yield an effective picture of this complex data. The best that can be done is something such as that shown in Fig. 4, which is a three-dimensional plot of the damping ratio vs the dimensionless resonant frequency parameter $\omega^2 d/a$ and the percentage of open sector area for a 45° sectored tank. The results presented are for three values of x_0/d, with water and methylene chloride as the test liquids. Maximum damping is produced for sectors with open areas of 16 to 23%. However, the excitation amplitude must be quite large to maintain the resonant frequency corresponding to solid-sector walls. Additional tests with sectors of smaller hole diameter ratios (d_h/d = 0.00139 and 0.00278) and open areas up to 23% increased the damping ratios to an average value of 0.15 while maintaining a frequency corresponding to the solid wall sector tank. Above 23% open area, the results become inconsistent in frequency and damping ratio.

Test results for 60° and 90° tanks with $d_h/d = 0.0056$ are also available. For the 60% sector tank, increased damping ratios at frequencies corresponding to the solid-sector wall exist only for open areas between 8 and 16% open area, depending on the excitation amplitude. Additional tests with $d_h/d = 0.00139$ and 0.00278 yielded mean damping ratios of approximately 0.12 at 16% to 23% open sector area, depending on excitation amplitude. The smaller open area corresponds to the lower excitation amplitudes. In the 90° tank, sectors with $d_h/d = 0.0056$ lose their compartmentation effect at small excitation amplitudes; however, tests with sector walls having $d_h/d = 0.00139$ and 0.00278 and up to 30% open area produced mean damping ratios of 0.12 at frequencies corresponding to the solid sector wall for $x_0/d = 0.00417$ and 0.00833. Tests at $x_0/d < 0.00417$ with $d_h/d = 0.00139$ gave results similar to the solid sector. The results for $d_h/d = 0.0279$ were inconclusive, and no consistent damping ratios or resonant frequencies were obtained.

Conclusions

Compartmentation of cylindrical tanks with *solid* walls is an effective means of increasing the lowest resonant frequency of the liquid. For large values of translational excitation amplitude, a significant decrease in resonant frequency exists. The liquid damping ratio with these solid-sector wall tanks averaged approximately 0.04. Compartmentation with *perforated* walls show less sensitivity to translational excitation amplitude, particularly for the tank with 45° sectors. However, for lower amplitudes, the resonant frequency decreased to a value that approximated the resonant frequency of an uncompartmented cylindrical tank for the three-sectored configurations. At the compartmented resonant frequencies, the liquid damping ratios were about 0.08 to 0.1. When the resonant frequencies approximated those attained in the uncompartmented tank, the highest liquid damping ratio increased to 0.2.

References

[1] Abramson, H. N., Garza, L. R., and Kana, D. D., "Some notes on liquid sloshing in compartmented cylindrical tanks," ARS J. **32**, 978–980 (1962).

[2] Bauer, H., "Liquid sloshing in a cylindrical quarter tank," AIAA J. **1**, 2601–2606 (1963).

[3] Bauer, H., "Liquid sloshing in a 45° sector compartmented cylindrical tank," AIAA J. **2**, 768–770 (1964).

[4] Abramson, H. N. and Ransleben, G. E., Jr., "Simulation of fuel sloshing characteristics in missile tanks by use of small models," ARS J. **30**, 603–612 (1960).

[5] Abramson, H. N., Chu, W.-H., and Garza, L. R., "Liquid sloshing in spherical tanks," AIAA J. **1**, 384–389 (1963).

[6] Abramson, H. N. and Garza, L. R., "Some measurements of the effects of ring baffles in cylindrical tanks," J. Spacecraft Rockets **1**, 560–562 (1964).

Interior Ballistics of Spinning Solid-Propellant Rockets

E. Karl Bastress*
Arthur D. Little, Inc., Cambridge, Mass.

Nomenclature

V = velocity
ω = angular velocity
r = radial distance from axis
D = diameter of motor
ϕ = parameter defined in Eq. (5)
a = sonic velocity
A = cross-sectional area
θ = spinning parameter defined in Eq. (10)
P = pressure
n = burning rate-pressure index
t_b = duration of burning

Superscripts

$(\ )^*$ = conditions at nozzle throat
$(\ )'$ = properties measured in spinning-coordinate system (unprimed properties measured in fixed coordinate system)

Subscripts

$(\ )_0$ = conditions at propellant burning surface
$(\ )_a$ = properties measured in axial direction
$(\ )_t$ = properties measured in tangential direction
$(\ )_\omega$ = ballistic properties of spinning motors

IN the development of spin-stabilized projectiles propelled by solid-propellant rocket motors, a number of cases have been observed wherein the apparent burning rates of spinning motors were substantially greater than those in similar motors fired in fixed test stands. Some observers have explained this phenomenon as being a result of erosive burning, but it is difficult to see how erosive burning conditions could be produced by spinning a motor. It is postulated here that the spinning motor establishes a vortex motion in the combustion gases which produces a reduction of the effective area of the

Received August 10, 1964; revision received November 30, 1964. This analysis was incidental to a study of gun-boosted rockets conducted for the Solid Rocket Propulsion Laboratory, Picatinny Arsenal.[1]

* Staff Associate, Division 500. Member AIAA.

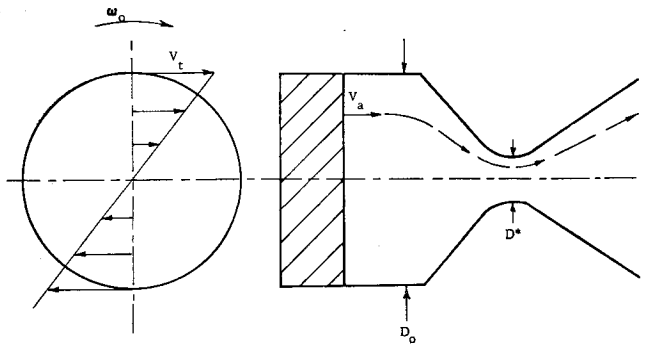

Fig. 1 End-burning model for analysis of spin effects.

nozzle throat and, hence, an increase in pressure and propellant burning rate.

It is assumed that an end-burning propellant grain is used with a single converging-diverging nozzle (Fig. 1). The motor spins about its longitudinal axis with a constant angular velocity ω_0, and combustion gases generated at an element of the propellant burning surface emerge with a tangential velocity component equal to that of the surface element. Within the constant-area portion of the combustion chamber, the velocity distribution is constant, and the flow can be described as "spinning-plug" flow. The axial velocity is constant, and the tangential velocity component varies as follows:

$$V_t = V_{t0} = \omega_0 r \tag{1}$$

With respect to a spinning-coordinate system, the flow in the chamber is one-dimensional, but as it enters the converging section of the nozzle, it is no longer one-dimensional. However, if the rate of change of cross-sectional area with length is small, the following assumptions are reasonably valid: 1) the flow is isentropic, and 2) the radial pressure gradient is negligible (a simple analysis will show that the radial pressure gradient caused by the spinning motion is small even at high rates of spin). It follows that the radial distribution of velocity will remain constant through the nozzle, since velocity is a unique function of pressure in isentropic flow, and a zero pressure gradient implies a zero velocity gradient. However, the angular momentum of the gases entering the nozzle will be preserved; hence tangential velocity of a streamtube must vary as follows:

$$V_t r = V_{t0} r_0 = \omega_0 r_0^2 \tag{2}$$

In isentropic flow, the contraction of streamtubes will be uniform, and the radial position of a streamtube will be a function of its radius of origin and the contraction ratio of the nozzle:

$$r/r_0 = D/D_0 \tag{3}$$

Substituting Eq. (3) into Eq. (2) gives

$$V_t = \omega_0 r_0^2/r = \omega_0 (D_0/D)^2 r \tag{4}$$

Thus, it is observed that the flow retains its "spinning-plug" character, but its angular velocity increases with the square of the contraction ratio (D_0/D) in order to preserve angular momentum.

If the flow is considered in the spinning-coordinate system, it is found to have a nonzero tangential velocity component in the nozzle:

$$V_t' = V_t - \omega_0 r = \omega_0 r (D_0/D)^2 - \omega_0 r \equiv \phi r \tag{5}$$

Since the total velocity is constant in any cross section of the nozzle, the axial velocity must be nonuniform:

$$V_a^2 = V'^2 - V_t'^2 = V'^2 - \phi^2 r^2 \tag{6}$$

Since the contraction of streamtubes is proportional to the nozzle contraction, sonic velocity will occur at the nozzle throat as in the nonspinning case, except that this velocity will have a tangential component. The axial velocity distribution at the throat is as follows:

$$V_a^* = (a^{*2} - \phi^{*2} r^2)^{1/2} \tag{7}$$

The fact that the axial throat velocity is subsonic, except at the nozzle axis, has the same effect as a reduction in throat area. An effective area for an element of the throat can be defined as follows:

$$\Delta A_{\text{eff}}^*/\Delta A^* = V_a^*/a^* = (1 - \phi^{*2} r^2/a^{*2})^{1/2} \tag{8}$$

By integration across the throat, the effective throat area can be found

$$\frac{A_{\text{eff}}^*}{A^*} = \frac{1}{A^*} \int_0^{D^*/2} 2\pi r \left(\frac{1 - \phi^{*2} r^2}{a^{*2}}\right)^{1/2} dr = \frac{2}{3\theta^2} [1 - (1 - \theta^2)^{3/2}] \tag{9}$$

where

$$\theta = \phi^* D^*/2a^* = (\omega_0 D^*/2a^*)[(Do/D^*)^2 - 1] \tag{10}$$

By series expansion of the bracketed term in Eq. (9), it can be shown that A_{eff}^*/A^* approaches unity as θ approaches zero. Thus, there is no effective area reduction for a nonspinning motor or for a throatless motor, as would be expected. Also, it is observed that the maximum value of θ satisfying Eq. (9) is unity. At this point the effective throat area is two-thirds the actual throat area. Manipulation of Eq. (10) indicates that θ is equal to the ratio of tangential velocity to sonic velocity at the nozzle surface:

$$\theta = (1/a^*)(V_t^* - \omega_0 r) = V_t'^*/a^* \quad \text{for} \quad r = D^*/2 \tag{11}$$

A value of θ equal to unity indicates that the axial velocity component at the surface of the throat is zero. From Eq. (10) it is apparent that θ is not limited physically to values below unity. Thus, this is a limitation of the analysis and not necessarily of the process. For values of θ greater than unity, the flow must take on a different configuration than that assumed here, and it is possible that the effective throat area is reduced still further. The variation of effective throat area with the parameter θ is shown in Fig. 2.

Making use of the internal ballistics equations for solid propellant rockets, the effects of spinning on chamber pressure can be determined:

$$P_\omega/P = (A^*/A_{\text{eff}}^*)^{1/(1-n)} \tag{12}$$

For rockets spinning at high rates, θ can approach unity. In this case, assuming a burning rate-pressure index $n = 0.3$, the chamber pressure will be increased by a factor of 1.8. Such a change would have a great, and possibly disastrous,

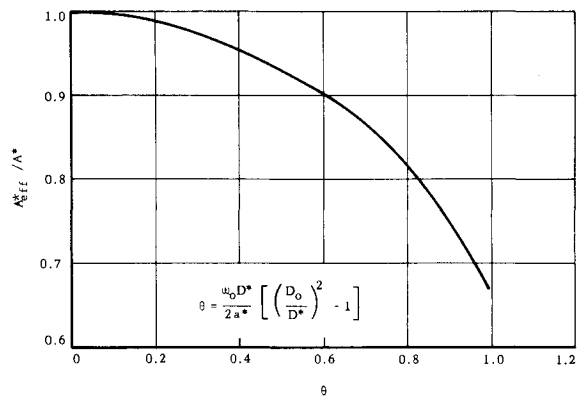

Fig. 2 Variation of effective throat area with spin rate.

effect on the performance of the motor if it were not expected. Thus, it is apparent that under some circumstances the effects of spin rate on motor performance can be significant.

The effect of motor spin rate on thrust and total impulse will be determined by the nozzle configuration. In the case of a convergent-divergent nozzle, the angular velocity of the combustion gases theoretically will decrease in the diverging section. If the diameter of the nozzle exit is equal to the chamber diameter, the exit velocity of the gases will be unaffected by the spin rate. In this case the instantaneous thrust would be increased because of the increased flow rate (for $n > 0$), but the total impulse would be unchanged.

Even though this analysis is highly idealized, it indicates the nature and approximate magnitude of the effect caused by spinning a solid-propellant motor with an end-burning grain. A similar analysis could be conducted for a motor with an internal-burning grain. In this case, the flow field would be more complex and time-dependent. For a simple, internal-burning cylindrical grain, all streamlines would emerge with equal angular momentum, and the field would be irrotational, or true vortex flow. An analysis of this condition has been carried out by Mager[2] who has shown that a reduction in effective throat area occurs as was found in the present case. A further complication to the problem would be the use of propellants whose combustion products contain condensed phases. If this case should warrant investigation, it might best be approached experimentally.

The implication of this analysis is that solid-propellant motors, which are intended to operate at high rates of spin, should be tested while spinning. Otherwise, actual performance characteristics may be significantly different from those observed during test firings.

References

[1] Allan, D. S., Bastress, E. K., and Knapton, D. A., "Design studies on a 105 mm gun boosted rocket," Final Report, Arthur D. Little, Inc., Contract No. DA-19-020-ORD-5695 (January 25, 1963); classified.

[2] Mager, A., "Approximate solution of isentropic swirling flow through a nozzle," ARS J. **31**, 1140–1148 (1961).

Spike Penetration Dynamics

GEORGE S. CAMPBELL*
University of Connecticut, Storrs, Conn.

THE use of nose spikes is a familiar technique for terminal recovery of missiles. Such a technique has a potential use for landing payloads on the moon or planets. It therefore seems appropriate to develop methods that will minimize the amount of empirical information used in the design of such a landing system. An extensive study of landing dynamics was reported in Ref. 1, a numerical technique was presented for estimating spike penetration, and a specific example was solved. In the present note, an analytical method is presented for making preliminary estimates of penetration and loads resulting from spike impact at speeds that are low compared with the sound speed in the solid material. Its accuracy remains to be checked by appropriate tests.

Analysis

The initial motion of a spike-landing device is calculated for application to landing-loads estimation. Initial motion is defined as the time between first ground contact and reversal of the spike tip's lateral motion. The spike approaches the ground with a vertical velocity component U_0 and a horizontal component V_0. The problem is simplified by assuming a truncated wedge shape for the spike (Fig. 1). Use of a more complicated, axially symmetric geometry does not appear warranted until the soil model assumed is subjected to experimental verification. The center of gravity of the body is located at x_c, y_c, and the tip of the spike is located at x_t, y_t. During the initial period of motion, the spike moves laterally in the positive Y direction simultaneously with its vertical penetration. The lateral velocity of the tip is approximately

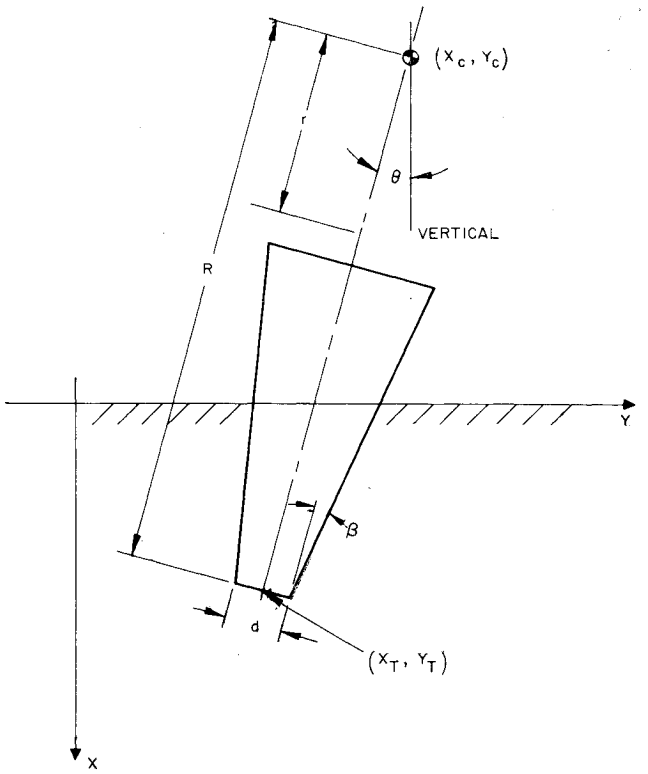

Fig. 1 Spike geometry.

$$v = V - R(d\theta/dt) \tag{1}$$

provided that $\theta \ll 1$. The end of the initial period is defined as the time at which v becomes zero. The vertical motion of the spike during the initial period is calculated from the relation†

$$\left.\begin{aligned}(d^2x_t/dt^2) + kx_t &= -K\\ k &= (\sigma L/m)(\tan\beta + \mu)\\ K &= \sigma Ld/m\end{aligned}\right\} \tag{2}$$

A bearing stress σ is assumed to act on the flat base and on the side that is moving in the Y direction. A frictional stress $\mu\sigma$ acts on one side of the spike. Consideration of forces on one side only is appropriate for slender spikes for which $\beta < \tan^{-1}(V_0/U_0)$. After the initial motion considered in this note, both sides of the wedge become effective in resisting penetration.

The bearing resistance σ depends on the shear strength of the soil.[2] Instantaneous soil strength may, in certain cases, be many times larger than values measured under static loading and should be used for estimating spike loads and trajectories. If the initial velocity is comparable to sound speed in the medium, resisting forces are expected to

Received August 31, 1964. The author wishes to express his appreciation to the Hughes Aircraft Company for their support of this work, which was performed on a consulting arrangement.

* Professor and Head of Aerospace Engineering Department. Associate Fellow Member AIAA.

† This is an approximate equation of motion, which neglects the difference between d^2x_c/dt^2 and d^2x_t/dt^2.